JOURNAL OF SPACECRAFT AND ROCKETS
Vol. 44, No. 5, September–October 2007

Aerogravity-Assist Maneuvers: Coupled Trajectory and Vehicle Shape Optimization

Roberto Armellin* and Michèle Lavagna†
Politecnico di Milano, 20156 Milano, Italy
and
Ryan P. Starkey‡ and Mark J. Lewis§
University of Maryland, College Park, Maryland 20742

DOI: 10.2514/1.28713

The aerogravity-assist maneuver is proposed as a tool to improve the efficiency of the gravity assist, because due to the interaction with the planetary atmosphere, the angular deviation of the velocity vector can be definitely increased. Even though the drag reduces the spacecraft velocity, the overall Δv gain could be substantial for a high-lift-to-drag vehicle. A previous study addressed the three-dimensional dynamic modeling and optimization of the maneuver, including heliocentric plane change, heating rate, and structural load analysis. A multidisciplinary study of aerogravity assist is proposed, focusing on coupled trajectory and vehicle shape optimization. A planar aerogravity assist of Mars is selected as a test case, with the aim of maximizing the vehicle heliocentric velocity and limiting the heating rate experienced during the atmospheric pass. A multiobjective approach is adopted, and a particle swarm optimization algorithm is chosen to detect the set of Pareto-optimal solutions. The study includes a further refinement of the trajectory for three significant shapes belonging to the Pareto curve. The associated optimal control problem is solved by selecting a direct-method approach. The dynamics are transcribed into a set of nonlinear constraints, and the arising nonlinear programming problem is solved through a sequential quadratic programming solver.

Nomenclature

A, B, C	=	power-law scaling parameters
C	=	Chapman–Rubisin parameter
C_D	=	drag coefficient
C_f	=	skin-friction coefficient
C_L	=	lift coefficient
C_p	=	pressure coefficient
c_p	=	specific heat at constant pressure, J/kg · K
D	=	drag force, N
g	=	acceleration of gravity, m/s^2
g_0	=	acceleration of gravity at the planet surface, m/s^2
H	=	total enthalpy, J/kg
h	=	altitude, km; enthalpy, J/kg
L	=	lift force, N
l	=	vehicle length, m
m	=	vehicle mass, kg
m, n	=	power-law exponents
$\hat{\boldsymbol{n}}$	=	unit vector normal to the panel surface
p	=	pressure, Pa
$\dot{q}$	=	heating rate, W/cm^2
R	=	distance from the planetary center of mass, m
Re	=	Reynolds number
R_0	=	planetary radius, m
r	=	Sutherland law exponent
r_n	=	nose and leading-edge bluntness radius, cm
S	=	vehicle surface, m^2
T	=	temperature, K
V	=	velocity, m/s
w	=	vehicle width, m
x, y, z	=	linear dimension, m
α	=	angle of attack, deg
β	=	shock angle, deg
δ	=	leading-edge inclination angle, overall bending angle, deg
ϵ	=	surface emissivity
φ	=	latitude, deg
γ	=	flight path angle, deg
Λ	=	sweep angle, deg
ψ	=	heading angle, deg
ρ	=	atmosphere density, kg/m^3
σ	=	bank angle, deg; Stefan–Boltzmann constant, 5.669×10^{-2} W/cm^2 · K^4
θ	=	vehicle centerline wedge angle, local surface incidence, deg
ϑ	=	longitude, deg

Subscripts

b	=	value for the base surface
CYL	=	cylinder value
e	=	property at the edge of the boundary layer
FP	=	flat-plate value
l	=	value for the lower surface
n	=	normal component
p	=	planform, planetary property
s	=	heliocentric value
t	=	tangential component
u	=	value for the upper surface
w	=	wall value
0	=	stagnation-point value
1	=	freestream condition
2	=	postshock condition
∞	=	freestream condition, value at the boundary of the sphere of influence

Presented as Paper 6036 at the AIAA/AAS Astrodynamics Specialists Conference, Keystone, CO, 21–24 August 2006; received 4 November 2006; revision received 28 November 2006; accepted for publication 6 May 2007.

*Postdoctoral Fellow, Department of Aerospace Engineering, Via La Masa 34; armellin@aero.polimi.it. Member AIAA.
†Assistant Professor, Department of Aerospace Engineering, Via La Masa 34; lavagna@aero.polimi.it. Member AIAA.
‡Research Scientist, Department of Aerospace Engineering, 3181 Glenn L. Martin Hall; rstarkey@umd.edu. Senior Member AIAA.
§Professor, Department of Aerospace Engineering, 3181 Glenn L. Martin Hall; lewis@eng.umd.edu. Fellow AIAA.

Superscripts

$+$ = after the gravity/aerogravity-assist maneuver
$-$ = before the gravity/aerogravity-assist maneuver

I. Introduction

PLANETARY gravity assist is a consolidated maneuver to limit the propellant mass required for interplanetary missions. This maneuver allows rotating the spacecraft relative velocity due to the momentum exchange occurring between the planet and the probe. Therefore, as a result, the outgoing heliocentric velocity vector can be controlled both in magnitude and direction. The momentum exchange depends on the eccentricity of the hyperbola described by the spacecraft in the planetary reference frame, which is a function of the spacecraft incoming velocity, the pericenter radius, and the planetary mass. The pericenter radius is, obviously, lower bounded by the planetary radius, and the spacecraft incoming velocity is generally high for high-energy missions; as a consequence, only massive planets allow great maneuver effectiveness. Unfortunately, only a few planets in the solar system satisfy this requirement.

The aerogravity assist (AGA) was first proposed by McRonald and Randolph [1] as a solution for the gravity-assist (GA) efficiency increase whenever planets with atmosphere are selected for the swingby. During an AGA maneuver, the spacecraft enters the planet atmosphere and exploits the aerodynamic force to augment the centripetal acceleration provided by the planet, allowing an increase in the overall velocity bending (i.e., the momentum exchange).

To maximize the AGA-maneuver effectiveness, the drag losses during the atmospheric path must be minimized. Therefore, the vehicle aerodynamics must provide a high lift-to-drag ratio (L/D) in hypersonic flying conditions. This goal can be reached by adopting waverider-shaped vehicles, first introduced by Nonweiler [2]. These vehicles' designs are aimed at keeping the shock wave attached to the leading edge and preserving the high pressure behind the shock along the bottom surface to obtain the so-called compression lift effect; high L/D ratios are hence obtained.

A considerable amount of work has been done on aerogravity-assist trajectory optimization with different levels of dynamic and control modeling. Earlier works adopted a simple analytical model and assumed a circular atmospheric path with no regard for optimality [3,4]. Lohar et al. [5] and Johnson and Longuski [6] presented a more realistic but 2-D mathematical model and obtained an optimal trajectory to maximize spacecraft heliocentric velocity. Other studies assumed an extended mathematical model: heating constraints were included and a 3-D trajectory was considered to exploit the maneuver for heliocentric plane change [7–9]. However, in the latter case, the constant-altitude approximation was still preserved. A 3-D dynamics model with no altitude constraint was addressed in Armellin et al. [10]. Either the angle-of-attack or the bank-angle profile was selected to control the atmospheric trajectory, and a wide set of constraints was considered. In all of these works, the vehicle aerodynamic properties were assumed as fixed and no more than a simple parametric analysis on the vehicle ballistic coefficient was carried out.

Since the late eighties, design optimization of waverider shapes has been the subject of several research projects. The University of Maryland hypersonics team produced a great amount of work about this topic, focusing on viscous [11], gas rarefaction [12], off-design conditions [13], and blunted-nose effects on L/D performances [14]. Furthermore, waveriders optimized for Cytherean and Martian atmosphere were carried out; the obtained solutions, optimal according to aerodynamics and shape, turned out to be definitely similar to the Earth-atmosphere-optimization scenario [15]. In most of these studies, vehicles were optimized for a specified design condition and little attention was given to the trajectory analysis.

A multidisciplinary approach for aerogravity-assist-maneuver design is proposed, focusing on coupled trajectory and vehicle shape optimization. A planar aerogravity assist of Mars is selected as the test case, with the aim of maximizing the vehicle heliocentric velocity and minimizing the heating rate experienced during the atmospheric path. Attention is focused on selecting those methods for the vehicle shape, dynamics, aerodynamics, and heating-rate description that showed a good compromise between accuracy and computational effort to be used in an optimization process. For the aerodynamic-properties estimation, different impact methods are applied for the different regions of the vehicle, and high-temperature effects are taken into account in the preliminary waverider design. A multiobjective approach is adopted, and a particle swarm optimization (PSO) tool is used to compute the Pareto curve. The study includes a further refinement of the trajectory for three significant configurations belonging to the Pareto curve. The associated optimal control problem is solved by selecting a direct-method approach. The dynamics are transcribed into a set of nonlinear constraints, and the arising nonlinear programming problem is solved with a sequential quadratic programming (SQP) solver.

The paper is organized as follows. First the dynamics, the configuration, the aerodynamics, and the heating-rate models are described. A parametric analysis for aerodynamic and heating rate is then proposed. The coupled vehicle/trajectory optimization is presented and results are discussed. As a conclusion, the trajectory refinement is analyzed.

II. Models

A. Dynamics

Two different sets of ordinary differential equations (ODEs) are chosen to describe the vehicle dynamics: a simple two-dimensional ODE to facilitate the solution of the coupled trajectory and vehicle shape optimization problem and a more complete set for the further refinement of the trajectory. The simplified model is described by the following equations:

$$\begin{cases} \dot{V} = -\frac{1}{2}\rho\frac{SC_D}{m}V^2 \\ \frac{V^2}{R} = g - \frac{1}{2}\rho\frac{SC_L}{m}V^2 \end{cases} \tag{1}$$

which describe the motions tangential and normal to the flight path, assuming a nearly circular atmospheric path. Within this approximation, g and ρ are considered constant.

With regard to the trajectory optimization refinement, the vehicle dynamics are written in a local noninertial reference frame x, y, z attached to the vehicle with the x axis aligned with the local vertical, y pointing toward east, and z completing the right-handed triad. An inertial planetocentric ecliptic reference frame X, Y, Z is assumed: in particular, the in-plane X axis is collinear to the vernal equinox direction. The relative orientation between the two frames is defined by the longitude ϑ and the latitude φ, whereas the flight path angle γ and the heading angle ψ are introduced to identify the vehicle velocity vector in the local reference frame. For the sake of clarity, these quantities are highlighted in Fig. 1. The motion of the vehicle's center of mass is described by the following set of ordinary differential equations:

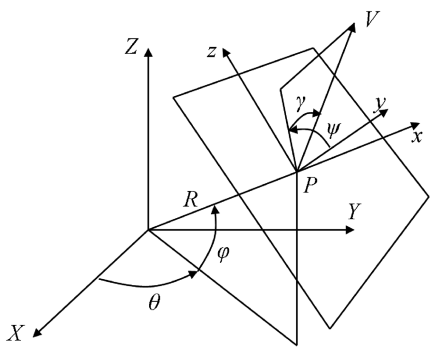

Fig. 1 Local reference frame and state vector variables $x = (R, \vartheta, \varphi, V, \gamma, \psi)$ definition.

$$\begin{cases} \dot{R} = V\sin\gamma \\ \dot{\vartheta} = \frac{V\cos\gamma\cos\psi}{R\cos\varphi} \\ \dot{\varphi} = \frac{V\cos\gamma\sin\psi}{R} \\ \dot{V} = \frac{D}{m} - g\sin\gamma \\ V\dot{\gamma} = \frac{L\cos\sigma}{m} - g\cos\gamma + \frac{V^2\cos\gamma}{R} \\ V\dot{\psi} = \frac{L\sin\sigma}{m\cos\gamma} - \frac{V^2\tan\varphi\cos\gamma\cos\psi}{R} \end{cases} \tag{2}$$

in which L and D are the lift and the drag forces, respectively, and σ is the bank angle, defined as the angle between the lift vector and the plane described by the local vertical and the velocity vector. The first three equations represent the kinematic relations, and the latter three represent the dynamics.

B. Shape Parametrization

The goal of the geometry definition is to describe a wide set of vehicle shapes with a limited set of variables. The waverider shape is described by means of six parameters (l, w, m, θ, δ, and n), as given in Starkey and Lewis [16]. The equations that describe the geometry are

$$\begin{gathered} y_p = Ax^n, \qquad z_u = (y_u/B)^{1/n} \\ z_l = x\tan\theta - \left(\frac{2yl_l^n}{wx^{n-m}}\right)^{1/m}(\tan\theta - \tan\delta) \end{gathered} \tag{3}$$

in which y_p describes the planform profile; z_u and z_l are the upper and lower surfaces, respectively; and A and B are two coefficients for which the value is given by $A = \frac{1}{2}w/l^n$ and $B = A/\tan^n\delta$. If $\delta < \theta$, the lower surface is convex, otherwise, it is concave. In the latter case, because the lower surface cannot cross the upper surface, a constraint on the slopes of the two surfaces at the planform boundary must be applied. An example of the geometry that can be obtained is given in Fig. 2 in which $C = Ax^{n-m}/(|\tan\theta - \tan\delta|)$. For a more detailed analysis of the shape definition, refer to Starkey and Lewis [16]. The reference surface for aerodynamic coefficients is given by the planform area $S_p = wl/(n+1)$. To limit the high heating rate due to the motion along the atmospheric path, the radius r_n is introduced to produce nose and leading-edge bluntness. This is accomplished by splitting the upper and lower surfaces of the vehicle and inserting the blunted portion between them. This procedure is preferable to carving out the blunted vehicle, because it increases the vehicle volume.

C. Aerodynamic Model

The aim of the aerodynamic model is to describe the aerodynamic properties of the shapes defined in the previous section for different flying conditions. The aerodynamic computation is carried out by a Fortran 90 code derived from the Hypersonic Arbitrary Body (HAB) program from Public Domain Aeronautical Software. This original version of the code takes as input the file describing the vehicle's geometry in Langley Wireframe Geometry Standard (LaWGS) format and allows computing of its aerodynamic performance by choosing a set of simplified impact methods. The major deficiency of the code is that both skin-friction and high-temperature effects are neglected; because these aspects are not negligible for AGA applications, a customization of the code was required.

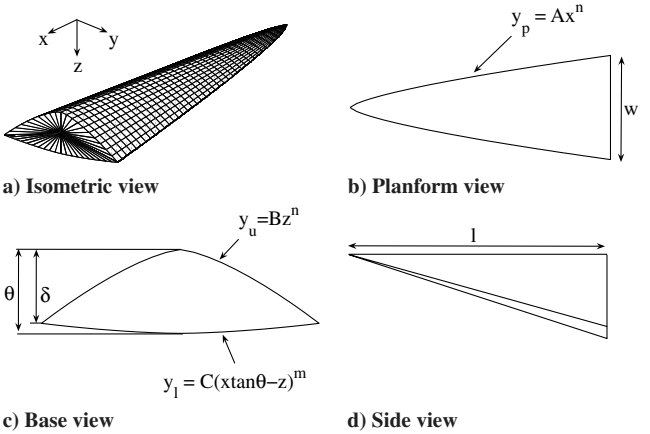

Fig. 2 Waverider shape parametrization.

The vehicle is divided into four regions and a different method for each of them is adopted to compute aerodynamic properties. The compression part of the vehicle is computed using modified Newtonian flow theory for highly tilted panels describing the nose and leading edge, whereas tangent-wedge approximation is assumed for the remaining panels belonging to the bottom surface. The high-Mach regime experienced during the atmospheric path causes the gas internal energy in the postshock region to be high enough to activate vibrational energy and dissociation. The NASA Chemical Equilibrium with Applications (CEA) code is used to deal with these effects [17]. This code computes the normal postshock properties of a gas in chemical equilibrium for arbitrary freestream gas mixture and flow conditions. Regarding the modified Newtonian flow, the pressure coefficient is given by

$$C_p = C_{p_0}\sin^2(\theta) \tag{4}$$

in which the stagnation-point pressure coefficient C_{p_0} is computed using CEA code [18]. With regard to the tangent-wedge approximation, the CEA is used to compute the component of the postshock velocity normal to the oblique shock V_{n_2}. To compute this value, an iterative procedure based on

$$\tan(\beta - \theta) = \frac{V_{n_2}}{V_{t_2}} \tag{5}$$

is implemented to determine the unknown shock angle β [18]. Dropping the calorically perfect gas approximation reduces the temperature ratio, whereas it increases the density and the pressure ratio across the shock. Furthermore, the normal shock-standoff distance and the shock angle in the tangent-wedge approximation reduce.

The pressure coefficient on the expansion surface is computed using Prandtl–Meyer theory. The empirical value $p_b = 0.45p_\infty$ is assumed for the base pressure, as reported in Gillum and Lewis [14].

As opposed to a blunt-body shape for which the skin-friction effect is negligible, pressure and skin-friction drag are of the same order of magnitude for a waverider application. The skin-friction value is computed assuming a laminar boundary layer by

$$C_f = \frac{0.664\sqrt{C_w p_e/p_\infty}}{\sqrt{Re_{x,\infty}}} \tag{6}$$

The laminar boundary-layer hypothesis is enforced by the high Mach number and relatively low Reynolds number experienced during the flight path. Using the perfect gas equation (which still holds for a chemical equilibrium mixture) [18], assuming constant pressure in the boundary layer, and adopting Sutherland's law for the viscosity, the Chapman–Rubisin parameter reduces to $(T_w/T_e)^{r-1}$, with $r = 0.75$. The properties at the edge of the boundary layer are given by the postshock conditions. Three different values of wall temperature (3000, 1200, and 500 K) are considered for the leading edge and nose, bottom surface, and upper and base surfaces, respectively. It is observed that the skin-friction sensitivity to the wall temperature is low and that the values assumed lead to a conservative approach, because they overestimate the skin-friction magnitude. For each panel describing the vehicle's shape, the friction direction is computed by $-(\boldsymbol{V}\times\hat{\boldsymbol{n}})\times\hat{\boldsymbol{n}}$ [19].

D. Heating Rates and Wall Temperature

The heating rate experienced by the vehicle during the atmospheric path represents one of the major issues connected with the

AGA-maneuver design. Indeed, the combined effects of high velocity and sharp nose and leading edge cause high convective fluxes. The amount of heat and the associated radiative equilibrium wall temperature are computed for three regions of interest only (i.e., vehicle nose, leading edge, and ventral centerline). The heating value is computed using stagnation, finite sweep cylinder, and flat-plate-heating theory [20]. Furthermore, radiative heating is considered for the stagnation point [20]. For more clarity, the formulas used are reported next.

The convective stagnation-point heating is calculated using the relation

$$\dot{q}_{w_0} = 1.35(10^{-8})\left(\frac{\rho}{r_n}\right)^{1/2} V^{3.04}\left(1-\frac{h_w}{H}\right) \tag{7}$$

The leading-edge heating rate is computed with

$$\dot{q}_{w_{\mathrm{LE}}} = \left(\dot{q}^2_{w_{\mathrm{CYL}}} + \dot{q}^2_{w_{\mathrm{FP}}}\sin^2\Lambda\right)^{0.5}\cos\alpha \tag{8}$$

where $\dot{q}_{w_{\mathrm{CYL}}}$ is given by

$$\dot{q}_{w_{\mathrm{CYL}}} = 0.955(10^{-8})\left(\frac{\rho}{r_n}\right)^{1/2} V^{3.04}(1-0.2\sin^2\Lambda)(\cos\Lambda)\left(1-\frac{h_w}{h_{aw}}\right) \tag{9}$$

and

$$h_{aw} = h_\infty + (1-0.2\sin^2\Lambda)\frac{V^2}{2}$$

The flat-plate laminar heating contribution in Eq. (8) has the expression

$$\dot{q}_{w_{\mathrm{FP}}} = 1.87(10^{-9})\left(\frac{\rho\cos\theta_{\mathrm{FP}}}{x}\right)^{1/2} V^{3.04}(\sin\theta_{\mathrm{FP}})\left(1-\frac{h_w}{h_{aw}}\right) \tag{10}$$

where θ_{FP} is the flat-plate angle of attack. For the leading edge, $\theta_{\mathrm{FP}} = 90\,\mathrm{deg} - \Lambda$. The relations (7–10) give the value for the heating rate in watts per square centimeter. Note that all of these relations are based on a fully catalytic wall assumption, which is a conservative approach, as stated in Tauber and Bowles [20]. Finally, the radiative heat flux is estimated by

$$q_r = F r_n^a \rho^p f(V) \tag{11}$$

in which $f(V)$ are tabulated data depending upon the vehicle velocity and the atmosphere chemical composition [21], and the remaining quantities values are

$$F = 4.736\times 10^4, \qquad a = 1.072\times 10^6 V^{-1.88}\rho^{-0.325}$$
$$p = 1.22$$

Wall temperatures for each of the three regions are estimated through local radiative equilibrium (i.e., neglecting conduction as well as thermal inertia). The temperature is given by

$$T_w = \left(\frac{\dot{q}}{\varepsilon\sigma}\right)^{0.25} \tag{12}$$

where $\dot{q}$ represents the appropriate value of the heating rate affecting each region. Because the wall enthalpy $h_w = c_p T_w$ depends on the wall temperature, an iteration procedure is required to compute the T_w value. Ultrahigh-temperature ceramic (UHTC) material is selected as the wall material, with $c_p = 795\ \mathrm{J/kg\cdot K}$ and $T_{\max} = 3033\ \mathrm{K}$.¶

¶Data available online at http://cobweb.ecn.purdue.edu/~aae450s/methods.pdf [retrieved 14 June 2007].

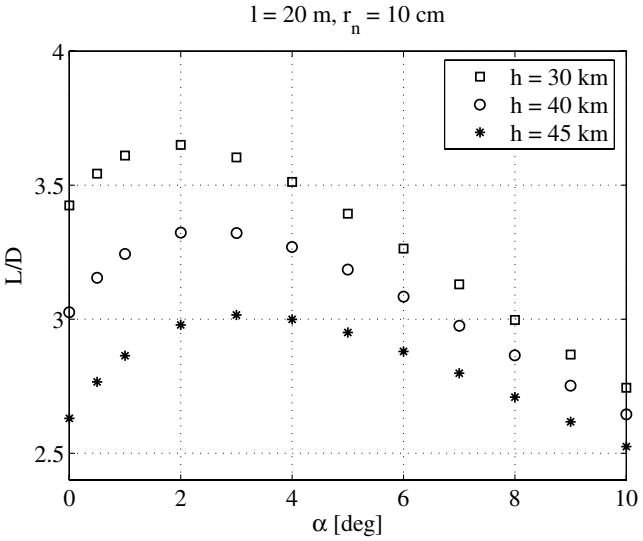

Fig. 3 Flying-altitude effect.

III. Aerodynamic and Heating-Rate Parametric Analysis

Before analyzing the coupled trajectory and shape optimization, a parametric study on the effects of the vehicle shape and flying altitude on aerodynamics and heating rates is performed. The stagnation heating rate is analyzed first.

As can be easily understood by Eq. (7), the stagnation heating decreases by increasing the nose bluntness and the flying altitude. Furthermore, from Eq. (8) it can be seen that a slender vehicle allows the leading-edge heating to decrease.

The dependence of the aerodynamic performance with both geometric and altitude variables is not as immediate as for the heating rate, because an analytical formula is not available. For this reason, a more detailed analysis is performed, focusing on vehicle length, flying altitude, and nose-bluntness effect on L/D ratio. Flying altitude is considered first. As can be seen from Fig. 3, the flying altitude has a considerable effect on the L/D performance. This sensitivity is due to the exponential change of the density with the altitude, which effects the skin-friction value through the Reynolds number. In past works, it has been stated that to reduce the heating rate, the vehicle should fly at high altitude. This analysis reveals that as a counterpoint, flying at high altitude decreases the aerodynamic performance and, consequently, increases the drag losses. In Fig. 4,

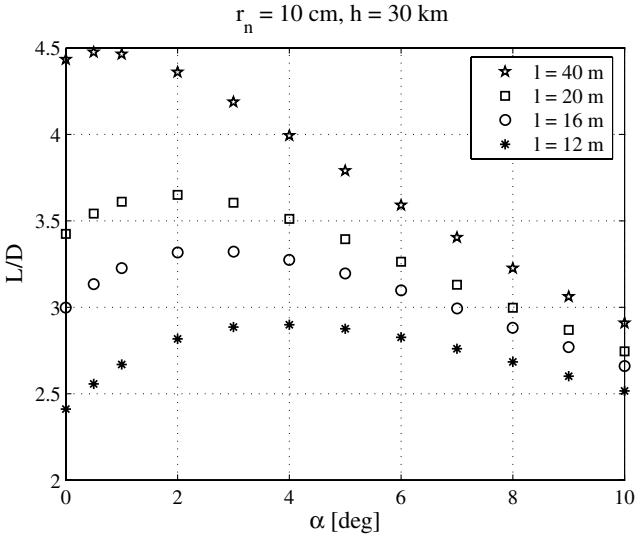

Fig. 4 Vehicle-length effect.

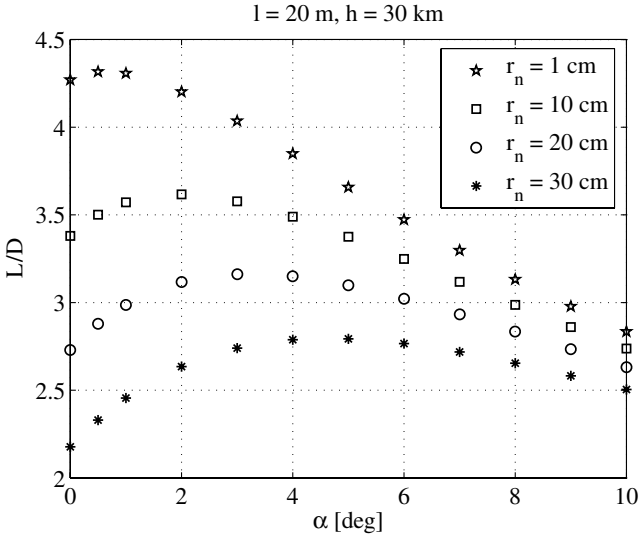

Fig. 5 Nose and leading-edge bluntness effect.

the effect of vehicle length is plotted. The L/D performance increases with vehicle length for two main reasons. For a longer vehicle, the skin-friction effect lowers because the local Reynolds number is large for a greater part of the vehicle. Furthermore, increasing the vehicle length reduces the impact of nose and leading-edge bluntness. Finally, the effect of nose and leading-edge bluntness is depicted in Fig. 5. As expected, a sharper vehicle is characterized by a higher value of L/D. Increasing the bluntness has the coupled effect of reducing the aerodynamic performance, due to high pressure on the forebody of the vehicle, and shifting the L/D maximum to a greater angle of attack.

As shown in Table 1, apart from the maximum slenderness commonality, maximizing L/D (i.e., maximizing V_s^+) and containing the heating rates are two competing goals. As a result, a tradeoff between the two performance indexes arises.

IV. Coupled Trajectory and Vehicle Shape Optimization

Because the maximization of heliocentric velocity V_s^+ and the minimization of the heating rate experienced by the vehicle are two competing requirements, a multiobjective optimization architecture is adopted. A particle swarm optimization (PSO) algorithm is chosen to detect the set of Pareto dominant solutions. PSO is initialized with a group of random particles (solutions) and then searches for optima by updating generations. In every iteration, each particle is updated by following the two *best* values. The first one is the best solution (fitness) that has been achieved so far. Another *best* value that is tracked by the particle swarm optimizer is the best value obtained so far by any particle in the population. The particle then updates its position on the basis of the two best values found [22]. The optimization process carries on until the algorithm converges.

Table 1 Aerodynamic and heating-rate parametric-analysis conclusions

	$L/D \uparrow$	$\dot{q} \downarrow$
l	↑	–
r_n	↓	↑
h	↓	↑
Slenderness	↑	↑

In the following discussion, the optimization architecture is given, following the scheme given in Fig. 6. The optimization variable vector is given by the geometric variables and equilibrium altitude (i.e., $l^{15\text{–}20\,\mathrm{m}}$, $w^{4\text{–}10\,\mathrm{m}}$, $\theta^{4\text{–}6\,\mathrm{deg}}$, $\delta^{6\text{–}20\,\mathrm{deg}}$, $m^{0.1\text{–}0.9}$, $n^{0.1\text{–}0.9}$, $r_n^{1\text{–}30\,\mathrm{cm}}$, and $h^{30\text{–}40\,\mathrm{km}}$), where the superscripts indicate the design space. The vehicle density and the initial incoming velocity in the atmosphere are considered as parameters. A vehicle density of 80 $\mathrm{kg/m^3}$ and an initial velocity at the atmosphere boundary corresponding to $V_\infty = 10,000$ m/s are considered. The angle between the sphere of influence incoming velocity V_∞^- and Mars velocity V_p is 102 deg (this value is taken from an external interplanetary trajectory optimization code).

The final heliocentric velocity calculation requires the following steps. The aerodynamic properties are computed using the model explained in Sec. II.C for different angles of attack and the vehicle C_L–C_D curve is obtained. The vehicle volume is computed numerically, and the vehicle mass is obtained by multiplying the volume for the vehicle density. From the radial dynamics, the C_L required to maintain the equilibrium altitude h is computed, then the C_L–C_D curve determines the associated value of C_D. The tangential dynamics are integrated until the bending angle that guarantees the maximum heliocentric velocity V_s^+ is reached. The overall bending angle δ obtained through the maneuver is given by the sum of three components: namely, the deflection due to the two hyperbolic arches, supplemented by the atmospheric bending. Note that in this simplified approach, it is supposed that no atmosphere is encountered until the equilibrium altitude is reached. This simplification is acceptable because, as will be shown in the next section, the equilibrium altitude is reached through a fast passage in the higher part of the atmosphere. Given the equilibrium altitude and the vehicle nose bluntness, the stagnation-point heating rate can be computed using Eq. (7). Once the two performance indexes are computed, the particle swarm optimizer iterates until the set of Pareto-optimal solutions is computed.

Figure 7 shows the solution set, from which it can be easily seen that lowering the heating rate and maximizing the heliocentric velocity are two competing goals. The multiobjective optimization allows the designer to select, from among all of the Pareto-optimal solutions, those solutions that are most representative of his goals. In this case, three different solutions are taken: one that maximizes the heliocentric velocity, one that minimizes the heating rate, and an intermediate one.

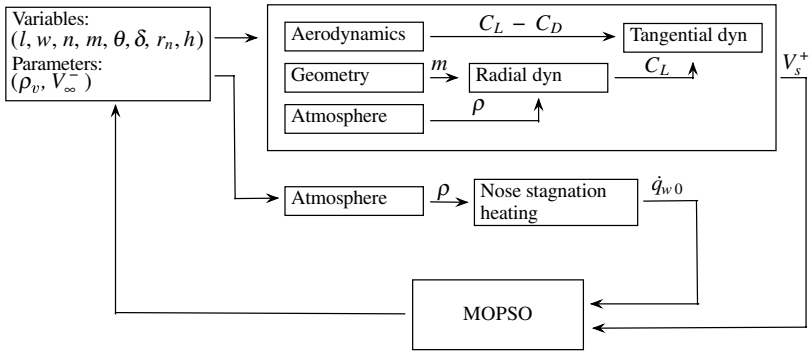

Fig. 6 Optimization flow chart.

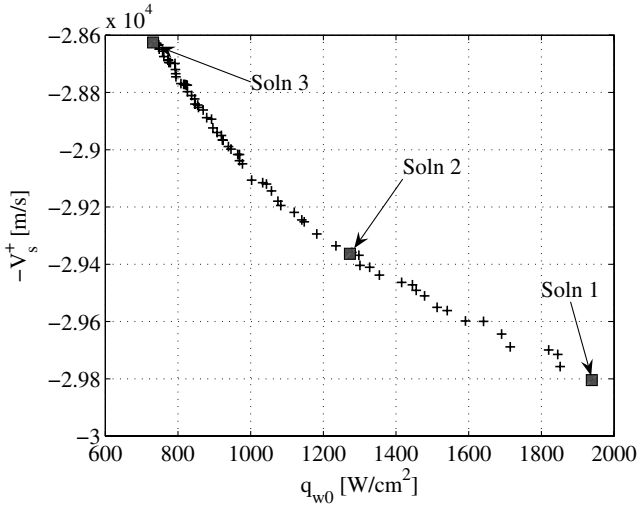

Fig. 7 Optimization Pareto front.

As shown by Fig. 8 and Table 2, the configuration that maximizes the heliocentric velocity is characterized by the smallest value of nose bluntness and lowest equilibrium altitude. Conversely, the heating-rate-oriented solution shows the greatest value of nose bluntness and the highest equilibrium altitude. The intermediate solution has averaged properties. All of the vehicles tend to be long and sharp. Table 2 contains the most important results of the optimization, including the optimal bending angle and the maximum L/D for each shape.

V. Trajectory Refinement

The coupled shape and trajectory optimization relies on a very simplified dynamical model. As a counterpoint with a limited computational effort, the main features of AGA maneuver (i.e., the final velocity V_s^+, the overall bending angle, and the equilibrium altitude) are computed with good approximation. To better evaluate the maneuver performance, a trajectory refinement is carried out. The trajectory refinement computes, for a given vehicle shape, the optimal guidance that maximizes the heliocentric velocity and satisfies the heating-rate constraint. The three shapes described in the previous section are analyzed. For each shape, the associated heating rate given in the Pareto curve in Fig. 7 is considered as the maximum value allowed in the trajectory refinement. Because a planar maneuver is of concern, only the ratio $\lambda = C_L/C_{L_{(L/D)_{\max}}}$ is considered as a control variable, whereas the bank angle is fixed to zero during the whole trajectory. The aerodynamic properties of each vehicle are obtained by interpolating the values given by the aerodynamic module used for the coupled trajectory and shape optimization. The C_D depends on C_L by

$$C_D = p_1 C_L^2 + p_2 C_L + p_3 \tag{14}$$

in which p_i coefficients are obtained by a least-squares method. An additional parameter is considered to take into account performance changes with altitude.

The optimal control problem is solved with a direct method in which the dynamics are transcribed into a set of nonlinear constraint with a multiple-shooting technique. The resulting nonlinear programming is solved using a sequential quadratic programming (SQP) optimizer. For a detailed description of the method, see Armellin et al. [10].

Figure 9 shows the altitude profile for the three selected configurations. Considering that R in Eq. (1) includes also Mars's radius, it easy to accept that the constant-altitude approximation made in the previous section is acceptable for the bulk of the trajectory. Also, comparing the equilibrium altitude profile with the results of the simplified model, it can be noticed that a good agreement is reached. As a main difference, dropping the approximation of constant altitude (i.e., flying at a variable angle of attack) allows the vehicle to go deeper in the atmosphere as soon as the velocity magnitude has correctly reduced, according to the heating-rate limit. This effect is clear for the third solution, for which the estimated altitude is 40 km. In the refined trajectory, this value is kept only at the beginning of the trajectory, in which the heating constraint is active. Subsequently, the vehicle changes its angle of attack to fly deeper in the atmosphere at maximum L/D.

The minus sign of λ in Fig. 10 means that the three vehicles fly upside down, and the $\lambda \approx -1$ for the bulk of the trajectory indicates that the trajectories are flown at a near-maximum L/D ratio. Figure 11 shows the velocity loss due to drag. The greater the L/D ratio, the lower the velocity loss, even if a longer duration in the atmosphere is selected by the optimizer. Figure 12 demonstrates the trajectories in the planetocentric reference frame, and Fig. 13 shows the associate velocity vectors. The overall velocity bending is such that the V_s^+ (the sum of V_∞^+ and V_p) is maximized, and this does not translate into alignment of the planet and spacecraft velocities. A larger bending angle demand requires the vehicle to pass through the atmosphere longer, increasing the velocity loss due to drag. In particular, a lower L/D vehicle is characterized by a smaller atmosphere trajectory duration. Even though the atmosphere interaction lowers the sphere of influence of outgoing velocity, the AGA maneuver, for all three shapes considered, increases the final heliocentric velocity reachable with a GA, as shown in Table 3. Note that the values of V_s^+ of Table 3 are in good agreement with those shown in Table 2. A general increase is achieved with the trajectory refinement, which proves the effectiveness of the optimized control guidance.

The temperature for the nose, leading edge, and ventral centerline are obtained with the method described in Sec. II.D. Only the results for the first and second solutions are shown in Figs. 14–17. The value at 0 in the leading-edge axis corresponds to the temperature at the stagnation point. The highest temperatures are reached at the stagnation point when the vehicle flies at the lowest altitude in the atmosphere with almost the entire entry velocity magnitude. The velocity loss due to drag interaction then causes a rapid decrease of heating rate and, consequently, of the temperature. The temperature value for the ventral centerlines is noticeably lower due to the small angle of attack of the ventral surface apart from the forebody of the vehicle. Note that for both configurations, the wall-temperature peak in the stagnation region exceeds the maximum value allowed by the state-of-art materials, but for solution 3, this value is not far from the present technology. Furthermore, the methods used for both the heating rate and the wall temperature overestimate the actual values, for the reason detailed in Sec. II.D.

VI. Conclusions

A multidisciplinary approach is proposed to analyze aerogravity-assist trajectories on Mars in more detail. The models adopted for dynamics, configuration, aerodynamics, and heating rates enable the implementation of multiobjective coupled trajectory and vehicle shape optimization. Although very simplified, the dynamical model

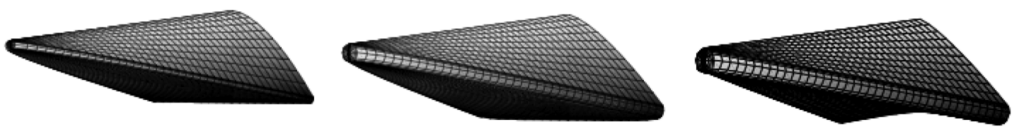

Fig. 8 Waverider shapes for Soln 1, Soln 2, and Soln 3 (from left to right).

Table 2 Coupled trajectory and shape optimization: results for the three selected configurations

	l, m	w, m	r_n, cm	h, km	δ, deg	$(L/D)_{\max}$	V_s^+, m/s	$\dot{q}$, W/cm^2
Soln 1	20	4.1509	10	30	77.78	3.56	29,808	1998.3
Soln 2	19.8065	4.8170	21	32.64	73.52	2.95	29,359	1311.4
Soln 3	19.6913	4.4652	30	40	66.50	2.33	28,632	741

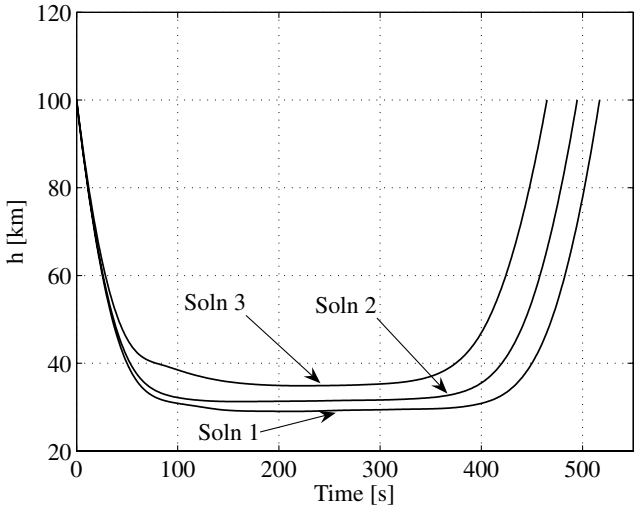

Fig. 9 Altitude profile.

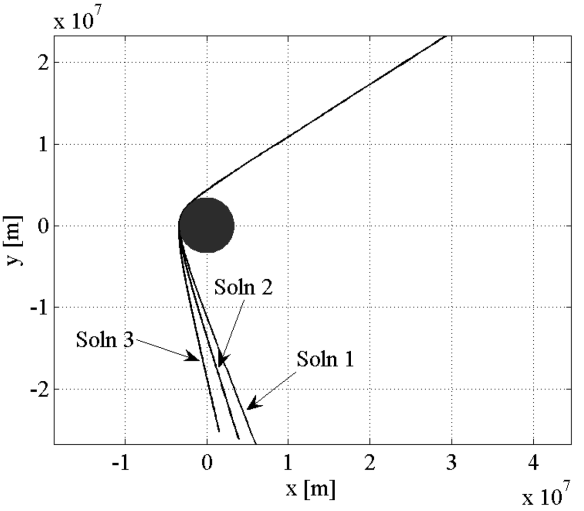

Fig. 12 AGA maneuver: planetocentric trajectory.

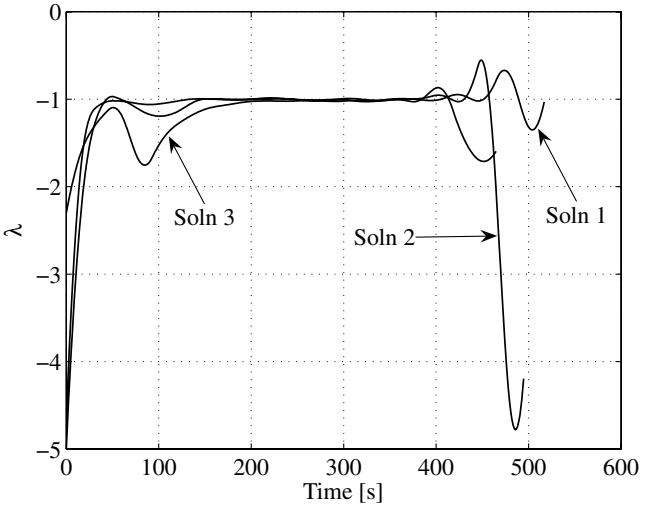

Fig. 10 Control-variable profile.

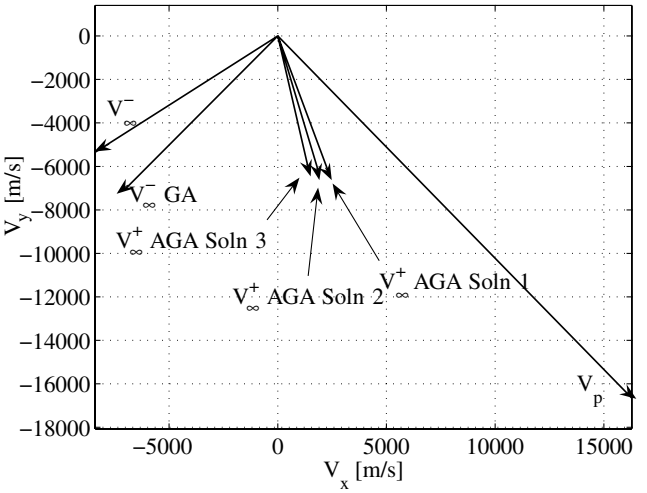

Fig. 13 AGA maneuver: velocity vectors.

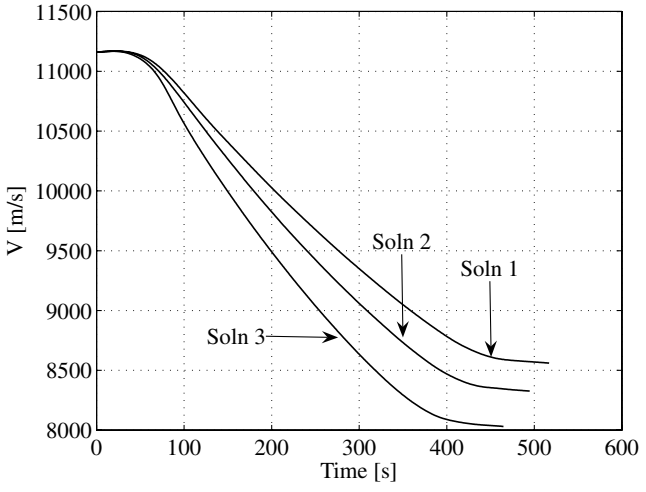

Fig. 11 Velocity magnitude.

addresses two important aspects of AGA trajectory: an estimate of the trajectory equilibrium altitude and the computation of the final heliocentric velocity. The trajectory refinement thus improves the solutions calculated, increasing the V_s^+. The aerodynamic description devises the aerodynamic properties of different sets of configuration and different flying conditions, including high-temperature effects.

Table 3 AGA trajectory refinement: results and GA comparison

		Soln 1	Soln 2	Soln 3	GA
V_∞^-	m/s	10,000	10,000	10,000	10,000
V_s^-	m/s	23,378	23,378	23,378	23,378
V_∞^+	m/s	6981.8	6692.9	6321.4	10000
V_s^+	m/s	29,857	29,439	28,898	25,454
$q_{w0,\max}$	W/cm^2	1851.6	1250.3	723.7	——
δ	deg	78.89	75.22	70.69	12.5

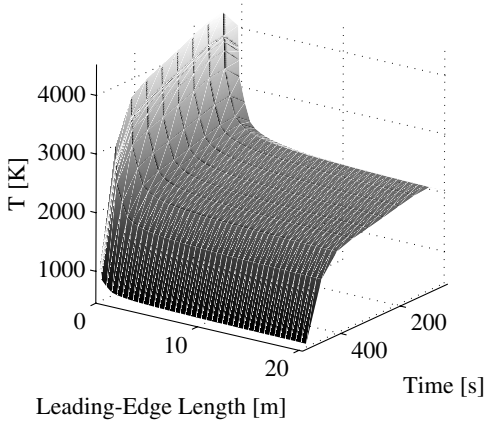

Fig. 14 Soln 1 leading-edge temperature.

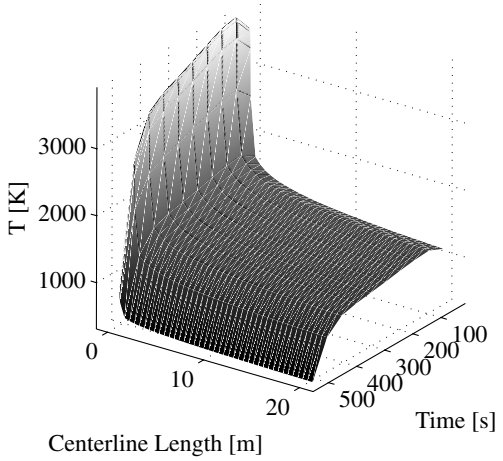

Fig. 15 Soln 1 ventral-centerline temperature.

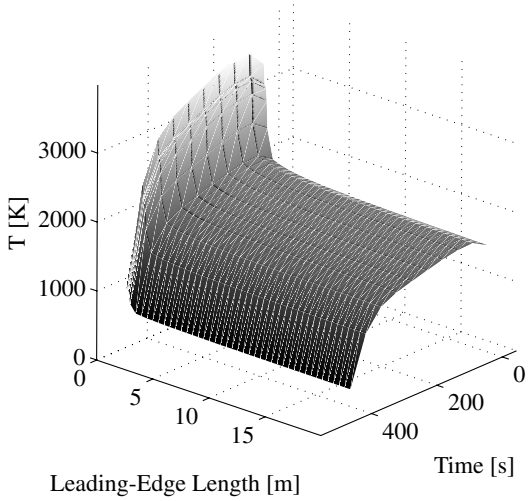

Fig. 16 Soln 3 leading-edge temperature.

The tradeoff between heliocentric velocity maximization and heating-rate limitation is analyzed in detail. High leading-edge bluntness must be adopted to limit the heating rate affecting the vehicle. Because of the vehicle's high-velocity and low-altitude requirements, a 30-cm nose and leading-edge blunted vehicle cannot withstand the high temperature reached using state-of-the-art materials if no active cooling is used. Vehicles with a maximum value of L/D of 2.33 still allow the heliocentric velocity to increase with respect to an GA maneuver. AGA maneuvers require long and

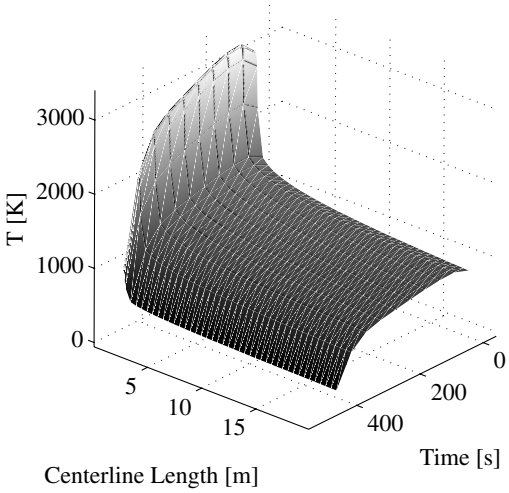

Fig. 17 Soln 3 ventral-centerline temperature.

slender waveriders, which implies reconsidering the overall satellite design.

Acknowledgments

The authors would like to acknowledge the funding support of Carlo Gavazzi Space SpA.

References

[1] McRonald, A. D., and Randolph, J. E., "Hypersonic Maneuvering for Augmenting Planetary Gravity Assist," *Journal of Spacecraft and Rockets*, Vol. 29, No. 2, 1992, pp. 216–222.

[2] Nonweiler, T. R. F., "Delta Wings of Shapes Amenable to Exact Shock Wave Theory," *Journal of the Royal Aeronautical Society*, Vol. 67, No. 625, Jan. 1963, p. 39.

[3] Lewis, M. J., and McRonald, A. D., "Design of Hypersonic Waveriders for Aeroassisted Interplanetary Trajectories," *Journal of Spacecraft and Rockets*, Vol. 29, No. 5, 1992, pp. 653–660.

[4] Bonfiglio, E. P., Longusky, J. M., and Vinh, N. X., "Automated Design of Aerogravity-Assist Trajectories," *Journal of Spacecraft and Rockets*, Vol. 34, No. 6, 2000, pp. 768–775.

[5] Lohar, F. A., Mateescu, D., and Misra, A. K., "Optimal Atmospheric Trajectory for Aero-Gravity Assist," *Acta Astronautica* , Vol. 32, No. 2, 1994, pp. 89–96.

[6] Johnson, W. R., and Longuski, J. M., "Design of Aerogravity-Assist Trajectories," *Journal of Spacecraft and Rockets*, Vol. 39, No. 1, 2002, pp. 23–30.

[7] Lohar, F. A., Misra, A. K., and Mateescu, D., "Mars-Jupiter Aerogravity Assist Trajectories for High-Energy Transfer," *Journal of Spacecraft and Rockets*, Vol. 34, No. 1, 1997, pp. 16–21.

[8] Lohar, F. A., Mateescu, D., and Misra, A. K., "Optimal Aero-Gravity Assist with Heliocentric Plane Change," *Acta Astronautica*, Vol. 38, Nos. 4–8, 1996, pp. 445–456.

[9] Lohar, F. A., Misra, A. K., and Mateescu, D., "Optimal Atmospheric Trajectory for Aerogravity Assist with Heat Constraint," *Journal of Guidance, Control, and Dynamics*, Vol. 18, No. 4, 1995, pp. 723–730.

[10] Armellin, R., Lavagna, M., and Ercoli-Finzi, A., "Aero-Gravity Assist Maneuvers: Controlled Dynamics Modeling and Optimization," *Celestial Mechanics and Dynamical Astronomy*, Vol. 95, Nos. 1–4, May 2006, pp. 391–405.

[11] Bowcutt, K. G., Anderson, J. D., and Capriotti, D., "Viscous Optimized Hypersonic Waveriders," AIAA Paper 87-272, 1987.

[12] Anderson, J. D., Ferguson, F., and Lewis, M. J., "Hypersonic Waverider for High Altitude Applications," AIAA Paper 91-0530, 1991.

[13] Starkey, R. P., and Lewis, M. J., "Analytical Off-Design Lift-to-Drag-Ratio Analysis for Hypersonic Waveriders," *Journal of Spacecraft and Rockets*, Vol. 37, No. 5, 2000, pp. 684–691.

[14] Gillum, M. J., and Lewis, M. J., "Experimental Results on a Mach 14 Waverider with Blunt Leading Edges," *Journal of Aircraft*, Vol. 34, No. 3, 1997, pp. 296–303.

[15] Anderson, J. D., Lewis, M. J., Kothari, A. P., and Corda, S., "Hypersonic Waveriders for Planetary Atmospheres," *Journal of Spacecraft and Rockets*, Vol. 28, No. 4, 1991, pp. 401–410.

[16] Starkey, R. P., and Lewis, M. J., "Simple Analytical Model for Parametric Studies of Hypersonic Waveriders," *Journal of Spacecraft and Rockets*, Vol. 36, No. 4, 1999, pp. 516–523.

[17] McBride, B. J., and Gordon, S., "Computer Program for Calculation of Complex Chemical Equilibrium Compositions and Applications 2: User's Manual and Program Description," NASA Lewis Research Center, Rept. E-8017-1, Cleveland, OH, June 1996.

[18] Anderson, J. D., *Hypersonic and High Temperature Gas Dynamics*, McGraw–Hill, New York, 1989.

[19] Deters, K. J., "Preliminary Design Estimates of High-Speed Streamlines on Arbitrary Shaped Vehicles Defines by Quadrilateral Elements," AIAA Paper 93-3491, 1993.

[20] Tauber, M., and Bowles, J., "The Use of Atmospheric Braking During Mars Missions," AIAA Paper 89-1730, 1989.

[21] Tauber, M. E., and Sutton, K., "Stagnation-Point Radiative Heating Relations for Earth and Mars Entries," *Journal of Spacecraft and Rockets*, Vol. 28, No. 1, 1991, pp. 40–42.

[22] Parigini, C., Armellin, R., and Lavagna, M., "PSO Algorithm for Planetary Atmosphere Entry Vehicles Multidisciplinary Guidance Design," AIAA Paper 2006-6027, 2006.

D. Prabhu
Associate Editor